

<https://doi.org/10.1038/s43247-025-03120-4>

# Patterns in solar activity over the first millennium CE

Check for updates

Jian Wang<sup>1</sup> ✉, Michael W. Dee<sup>1</sup>, Benjamin J. S. Pope<sup>2</sup>, Mathew J. Owens<sup>3</sup>, David Brown<sup>4</sup>, Susanne Lindauer<sup>5</sup>, Kirsten Schwabe<sup>5</sup>, Hannes Knapp<sup>6</sup>, Thorsten Westphal<sup>6</sup> & Ronny Friedrich<sup>5</sup> ✉

Radiocarbon ( $^{14}\text{C}$ ) measurements are a powerful tool for reconstructing past solar activity and identifying extreme events caused by bursts of high-energy particles from the Sun. Such reconstructions improve understanding of long-term solar behaviour and the likelihood of hazardous particle events that are capable of disrupting modern technology. Here we present an annually resolved  $^{14}\text{C}$  record spanning 1 to 970 CE comprising five newly measured and three existing series from tree rings. The record is analysed with methods that combine statistical modelling of the carbon cycle, data-adaptive decomposition of solar cycles, and probabilistic detection of rapid  $^{14}\text{C}$  increases associated with energetic particle events. These analyses reveal four major intervals of reduced solar activity, two patterns in which the eleven-year cycle weakens then strengthens, and four candidate particle events in the years 14, 553, 675 and 954 CE.

Radiocarbon ( $^{14}\text{C}$ ) preserved in tree rings serves as an important archive for studying past solar activity. The rare isotope is produced in the upper atmosphere, when Galactic Cosmic Rays (GCR), modulated by solar magnetic and geomagnetic fields, collide with atmospheric atoms<sup>1</sup>. Once formed,  $^{14}\text{C}$  infiltrates all reservoirs of the carbon cycle, including plant matter via photosynthesis. Consequently, time series of  $^{14}\text{C}$  concentrations in annual tree rings reflect past changes in cosmic ray flux<sup>2</sup>. Since the 1950s, studies have shown that  $^{14}\text{C}$  variations in tree rings correlate with changes in solar activity. Low activity corresponds to increased  $^{14}\text{C}$  production, due to reduced solar shielding, and the opposite is true for periods of enhanced solar output<sup>3–5</sup>. Accordingly, the 11-year Schwabe cycle is also detectable in such  $^{14}\text{C}$  datasets<sup>6</sup>. Nowadays, improved measurement techniques<sup>7,8</sup> have facilitated the expansion of annual-resolution  $^{14}\text{C}$  records, greatly enhancing our ability to reconstruct both long-term and short-term solar variability<sup>9–14</sup>. Building on these advancements, recent studies have produced continuous high-resolution records for the second millennium CE and the final millennium BCE<sup>15,16</sup>, enabling quantitative reconstruction of the solar modulation parameter ( $\Phi$ ) and identification of Grand Solar Minima (GSM)—extended periods of reduced solar activity.

While considerable insights have already been gained using this method, unraveling the solar dynamo requires yet more precise  $^{14}\text{C}$  data and analysis. One key outstanding question is how the Schwabe cycle behaves during GSM. Combined with early sunspot records, it has been possible to reconstruct the

solar cycle during solar minimum to a certain extent<sup>17</sup>. In recent years, with more abundant and detailed records of cosmogenic isotopes many studies have suggested a weakened 11-year cycle exists across these periods<sup>10,15,18–20</sup>, reflecting possible changes in the meridional circulation and magnetic diffusivity profile of the solar convection zone<sup>21</sup>. To investigate this problem further, more GSM need to be identified. To date, only 4 of the 8 GSM implied by the coarse records have been confirmed by high-precision  $^{14}\text{C}$  data<sup>10,15,16,22</sup>. Another outstanding issue is how to extract the solar cycle signal during GSM. The most common methods employed involve applying bandpass filters<sup>9,10,15,16,19</sup> or subtracting a spline-fitted trend<sup>12</sup>. However, these approaches struggle to isolate the 11-year cycle reliably from other periodic components like the 22-year Hale cycle. Since variations in the Schwabe cycle itself are often the focus of the analysis, applying fixed filtering parameters may obfuscate key features of interest. Moreover, cycle length variability poses challenges to the filter's adaptability: for example, Miyahara et al.<sup>23</sup> reported a Schwabe cycle broadening to as long as 16 years prior to the Maunder Minimum. To address this, they proposed an alternative method based on curve-fitting with sinusoidal functions or fluctuation profiles derived from sunspot records. This approach can produce high-precision outputs, but it requires a large number of repeated single-ring measurements, which is too expensive for longer series. Moreover, the curve-fitting depends on sunspot observations – information that is unavailable for most of the pre-instrumental period<sup>23</sup>. Additionally, Usoskin et al. used the modeled

<sup>1</sup>Centre for Isotope Research, University of Groningen, Nijenborgh 6, 9747AG Groningen, the Netherlands. <sup>2</sup>School of Mathematical & Physical Sciences, Macquarie University, 12 Wally's Walk, Macquarie Park, NSW 2113, Australia. <sup>3</sup>Department of Meteorology, University of Reading, Earley Gate, Reading, RG6 6BB, UK. <sup>4</sup>School of Natural and Built Environment, The Queen's University, Belfast, BT7 1NN, UK. <sup>5</sup>Curt-Engelhorn-Center Archaeometry, D6, 3, 68159 Mannheim, Germany. <sup>6</sup>Laboratory of Dendroarchaeology, Department of Prehistoric Archaeology, University of Cologne, Weyertal 125, 50931 Cologne, Germany. ✉e-mail: [jian.wang@rug.nl](mailto:jian.wang@rug.nl); [ronny.friedrich@ceza.de](mailto:ronny.friedrich@ceza.de)

exponential relationship between  $^{14}\text{C}$  production and open solar flux (OSF), and an empirical algorithm to convert OSF to sunspot number, reconstructed the Schwabe cycles of the two Brehm datasets<sup>24,25</sup>. With a large number of Markov Chain Monte Carlo (MCMC) simulations, the method was able to resolve 35 out of 85 cycles in the first millennium BCE and 50 out of 96 cycles in the last millennium. However, the reconstruction of Schwabe cycle during GSM was not as good because the solar dynamo could be different from the model that was applied.

Another important challenge for  $^{14}\text{C}$  analysis is detecting abrupt spikes related to Solar Energetic Particle (SEP) events. First discovered in 2012<sup>26</sup>, six single-year increases in atmospheric  $^{14}\text{C}$  concentration (exceeding 10‰ in  $\Delta^{14}\text{C}$ ) have now been confirmed across the globe<sup>26–32</sup>. Although the originating mechanism of these so-called Miyake Events has not yet been established, it is widely believed they represent the extreme case of SEP events<sup>33,34</sup>. Here, it is worth noting that in comparing the occurrence frequency of Miyake events and directly observed SEP events (i.e., Ground Level Enhancements, GLEs), there appears to be a gap in the intermediate-energy range<sup>35</sup>. In terms of  $\Delta^{14}\text{C}$ , this gap may correspond to single-year rises that are between 4–10‰. Some such spikes have been already claimed<sup>15,36,37</sup> but as yet none have received global support<sup>38</sup>. While this ambiguity may relate to limitations in resolution or accuracy, the issue should be resolvable with the acquisition of more  $^{14}\text{C}$  data<sup>39</sup>.

In this study, we introduce eight annual  $^{14}\text{C}$  datasets from 1–970 CE, including five newly measured and three existing series<sup>9,11</sup>. These occupy the millennium between the periods covered by Brehm et al.<sup>15,16</sup>, effectively creating a continuous 3,000-year annual  $^{14}\text{C}$  archive. We adopt and refine several analytical methods to maximize the interpretive power of the dataset. These include Gaussian Process Regression (GPR) with control points for

carbon box modeling, Empirical Mode Decomposition (EMD) for cycle extraction, and Bayesian approaches for detecting rapid increases in  $^{14}\text{C}$ . Our goal is to offer a clearer, more detailed picture of solar behavior over the first millennium CE. Particular emphasis is placed on the identification of GSM, the behavior of the 11-year Schwabe cycle during GSM, and filling the gap related to intermediate-sized Miyake events.

## Results

### Comparison with IntCal20

The five newly measured single-year datasets encompass 852 of the total 961 years of our data set (Fig. 1a). Of these, 827 annual measurements were conducted on individual rings at the Curt-Engelhorn-Center Archaeometry in Mannheim, Germany, and 25 years (1–25 CE) were measured at the Centre for Isotope Research, University of Groningen, the Netherlands, ensuring an average analytical uncertainty of the new data is 1.72‰ with a state-of-art measurement system<sup>40,41</sup>. In addition, comparative measurements on identical tree rings were carried out at the Centre for Isotope Research with excellent agreement (see SI for quality control). As shown in Fig. 1a, our results lie mostly within  $2\sigma$  of the Northern Hemisphere international  $^{14}\text{C}$  reference record (IntCal20)<sup>42</sup>. Notably, two pronounced counter-phase offsets (1–40 CE, 820–840 CE) stand out (Fig. 1b), which is due to lower resolution data (from 3-year to 10-year resolution) used for these periods in IntCal20. Such disparities could result in inaccuracy in  $^{14}\text{C}$  dating, especially as they relate to the historical period. Another notable feature of the new data is that the measurements from 560 CE onward (excluding data from Park et al.<sup>11</sup>) are generally lower than IntCal20, showing offsets of  $-1.78 \pm 0.18\text{‰}$  and  $-2.22 \pm 0.19\text{‰}$  during 560–720 CE and 820–970 CE, respectively.

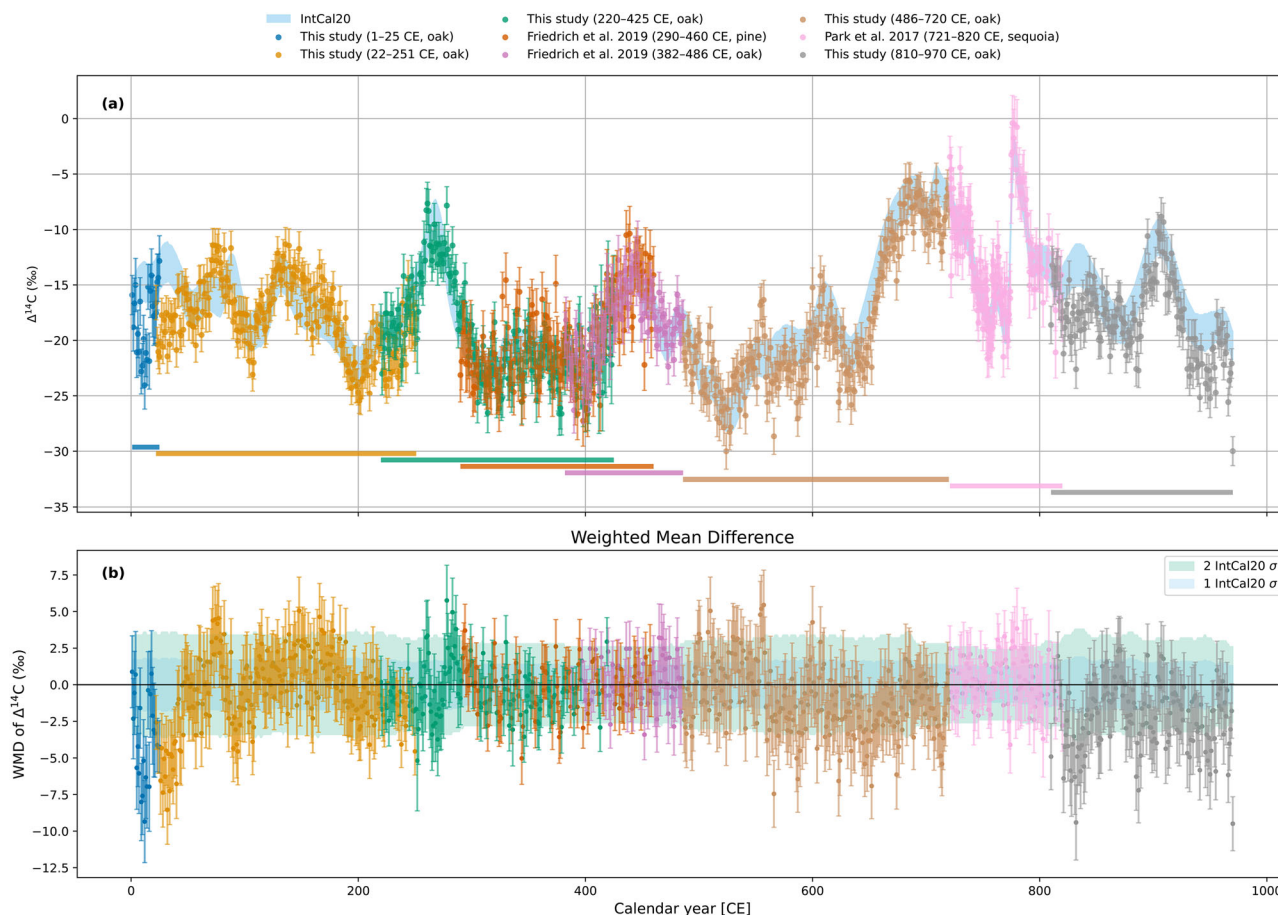


**Fig. 1 | Comparison of annual  $^{14}\text{C}$  datasets with IntCal20 from 1 to 970 CE (the error bars indicate the  $\pm 1\sigma$  measurement uncertainties). a** All eight datasets expressed in  $\Delta^{14}\text{C}$ , which represents the deviation of  $^{14}\text{C}$  content from a standard,

corrected for decay and fractionation. **b** The Weighted Mean Difference (WMD) between the seven datasets and IntCal20 of every measured year.

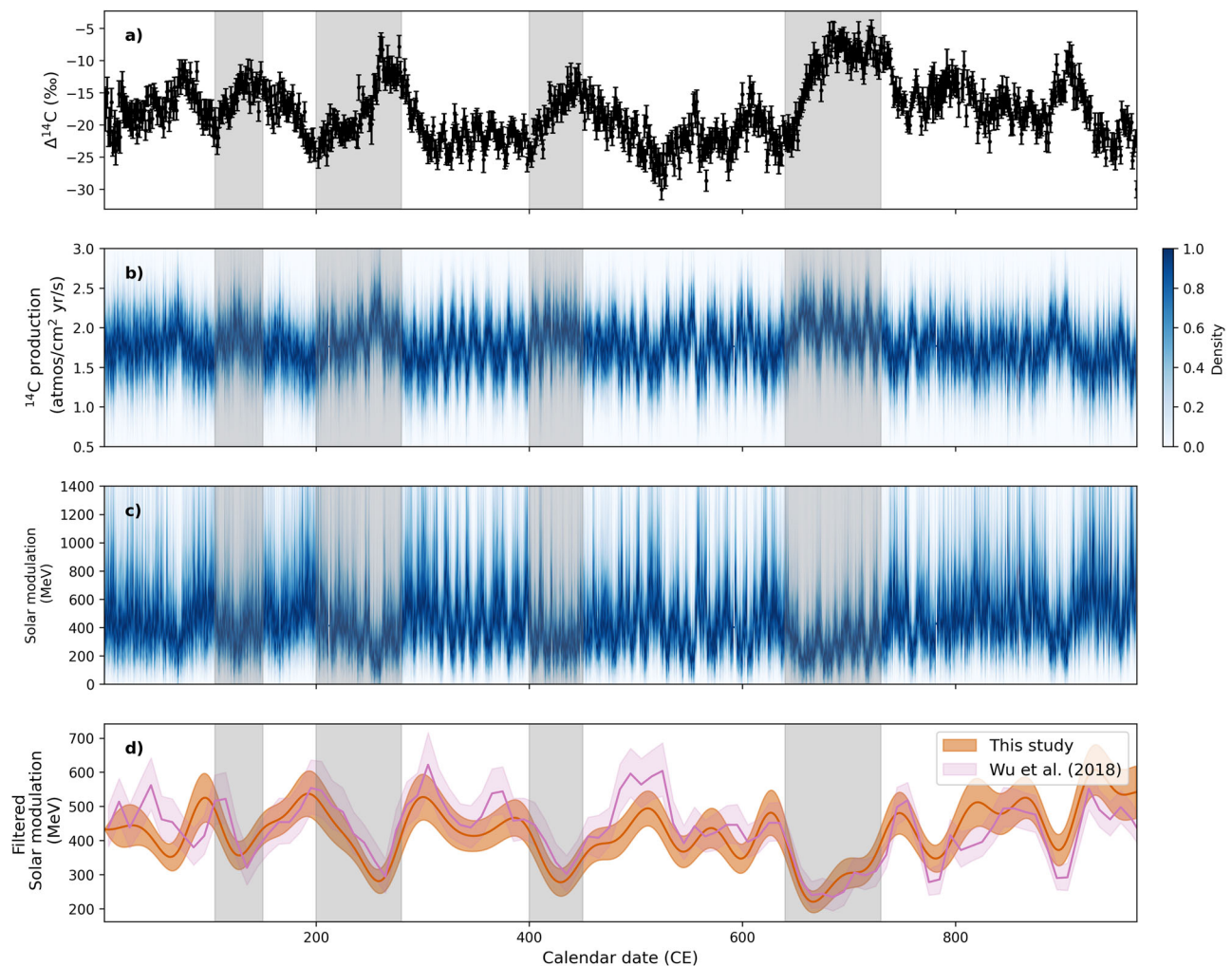


**Fig. 2 | Solar modulation parameter ( $\Phi$ ) reconstruction from the  $^{14}\text{C}$  dataset of 1–970 CE, with the four candidate GSM indicated in gray. **a** The single-year  $\Delta^{14}\text{C}$  data of 1–970 CE (775 CE spike detrended), and the error bars indicate the  $\pm 1\sigma$  measurement uncertainties. **b** The MCMC computed  $^{14}\text{C}$  production rate in 1–970 CE; the color bar indicates the probability density of the production rate. **c**  $\Phi$ .**

mapped from the  $^{14}\text{C}$  production rate and geomagnetic dipole moment records (the same color bar as in **b**). **d** 50-year lowpass filtered  $\Phi$  values that exhibit >95% probability density compared with the results of Wu et al.<sup>47</sup> with  $\pm 1\sigma$  computation uncertainties.

### Identification of Grand Solar Minima

The solar modulation parameter ( $\Phi$ ) quantifies the ability of the solar magnetic field to modulate GCR. A low and sustained  $\Phi$ —lasting several decades or even over a century—likely indicates a GSM.  $\Phi$  is typically derived from cosmogenic isotope production rates and geomagnetic dipole moment<sup>43–45</sup>. In this study, we applied a GPR with control points, and a MCMC scheme to estimate the  $^{14}\text{C}$  production rate using the carbon box model of Brehm et al.<sup>15</sup> at annual resolution. In addition, since the 775 CE Miyake Event is assumed to be related to an SEP strike, which is not correlated with either solar modulation or the Schwabe cycle<sup>34</sup>, this short-term rise was detrended from the original record (see Methods: Detrending the 775 Miyake Event and Fig. S5). Subsequently, we combined the production rate (Fig. 2b), record of geomagnetic dipole moment from Panovska et al.<sup>46</sup> (see SI, Fig. S10), and the mapping model from Kovaltsov et al.<sup>44</sup> to generate a probability distribution for  $\Phi$  (Fig. 2c). To align with existing results<sup>47</sup>, a 50-year low-pass filter was applied to the sequence of  $\Phi$  values with a probability density greater than 95%. The comparison between the two profiles for  $\Phi$  shows reasonable agreement (Fig. 2d), considering the offsets evident in the first 150 years of our dataset and the IntCal13 used in their computation<sup>48</sup>.

Using previously identified GSM as a guide<sup>15,16</sup>, this study proposes the existence of four GSM in the first millennium CE, one of which has already

been identified in many studies<sup>49–51</sup> and recently measured by Kudsk et al. with biannual resolution<sup>10</sup>. Although the definition of GSM is based on sunspot number (SSN) observation or SSN reconstruction with various cosmogenic isotope records<sup>47</sup>, and typically requires the group sunspot number to stay below 15 for at least 20 years<sup>50</sup>, we rely solely on the  $^{14}\text{C}$  record. To be conservative, three criteria were selected for a positive GSM identification: an overall rise in  $\Delta^{14}\text{C}$  rise ( $> 10\%$ ); a minimum in  $\Phi$  ( $< 400$  MeV), and an extended duration ( $> 40$  years). As summarized in Table 1, four periods meet these conditions (Fig. 2 and Tab. 1). Two are relatively short (105–150 CE; 400–450 CE), and are associated with moderate  $\Delta^{14}\text{C}$  increases (11.76% and 13.45%, respectively), which are comparable to the Dalton minimum. The other two (200–280 CE; 640–730 CE) are more sustained, with greater  $\Delta^{14}\text{C}$  increases (17.49% and 19.93%, respectively). Nevertheless, when compared to recent minima these can be classified as short or Maunder type<sup>50</sup>. Furthermore, the candidate GSM (640–730 CE), which was previously measured by Kudsk et al.<sup>10</sup>, who proposed the name ‘Horrebow Minimum’, actually appears to begin just prior to their  $^{14}\text{C}$  record. Another period of interest occurs from 885–908 CE, where  $\Delta^{14}\text{C}$  rises by 10% and  $\Phi$  falls well below 400 MeV. However, this feature is short-lived. It may indeed represent an extremely short GSM—similar to the profile in 5480 BCE described by Miyake et al.<sup>52</sup>—but further data would be required to verify this pattern.

**Table 1 | Summary of all the Grand Solar Minima identified by single-year  $^{14}\text{C}$  measurements<sup>15,16</sup> and the four new candidates found in this study (values shown in bold)**

Grand Solar Minima	Peak rise in $\Delta^{14}\text{C}$	$\phi$ (MeV)	Duration (yrs)
Dalton (1797–1823 CE)	10.62 $\pm$ 2.65‰	327–347	26
Maunder (1621–1718 CE)	21.32 $\pm$ 2.48‰	220–320	97
Spörer (1388–1558 CE)	26.22 $\pm$ 2.72‰	215–305	170
Wolf (1279–1349 CE)	14.55 $\pm$ 2.81‰	273–361	70
Oort (1021–1060 CE)	15.29 $\pm$ 2.01‰	332–381	39
<b>Horrebow (640–730 CE)</b>	<b>19.96 <math>\pm</math> 2.41‰</b>	<b>188–252</b>	<b>90</b>
<b>400–450 CE</b>	<b>13.45 <math>\pm</math> 1.86‰</b>	<b>237–318</b>	<b>40</b>
<b>200–280 CE</b>	<b>17.49 <math>\pm</math> 2.22‰</b>	<b>246–317</b>	<b>80</b>
<b>105–150 CE</b>	<b>11.76 <math>\pm</math> 2.11‰</b>	<b>302–404</b>	<b>45</b>
Platonic (413–325 BCE)	25.54 $\pm$ 2.48‰	296–352	88
Homeric (833–705 BCE)	24.11 $\pm$ 2.38‰	258–277	128

The peak rise in  $\Delta^{14}\text{C}$  is defined as the start and end point of its continuous increase during the GSM period. The uncertainties in the peak rise in  $\Delta^{14}\text{C}$  are estimated by the propagation of the measurement errors of the corresponding years. The duration of GSM proposed in this study is obtained by identifying when the solar modulation parameter ( $\phi$ ) starts to decrease and when it returns to the level evident before the decrease. In both Brehm et al. studies<sup>15,16</sup>, they used the Local Interstellar Spectrum (LIS) Model built by Herbst et al.<sup>43</sup>, while this study applied the LIS model used in Kovaltsov et al.<sup>44</sup>. To ensure the computed  $\phi$  is comparable, we applied the linear conversion proposed by Herbst et al.<sup>43</sup> to the results from Brehm et al.<sup>15,16</sup>. The conversion formula is:  $\phi_{\text{Brehm}} = 1.025 \cdot \phi_{\text{this study}} + 24.18$ .

### Schwabe cycle behavior during GSM

The solar cycle is a fundamental manifestation of solar activity, characterized by an 11-year (Schwabe) and a 22-year (Hale) quasi-periodicity, reflecting fluctuations in the solar magnetic field. However, the 11-year cycle is not fixed in length; sunspot records reveal variations ranging from approximately 8 to 14 years<sup>53–55</sup>. Analyzing these variations alongside Grand Solar Minima (GSM) can offer valuable insights into the solar dynamo mechanism<sup>30</sup> and improve our ability to anticipate the onset of GSM based on preceding solar cycle anomalies<sup>56,57</sup>. To accurately extract solar signals from  $^{14}\text{C}$  data, we applied EMD, a data-driven method capable of decomposing non-stationary and nonlinear time series into oscillatory components known as Intrinsic Mode Functions (IMFs)<sup>58</sup>. We first applied EMD to the raw  $\Delta^{14}\text{C}$  record (with the 775 CE spike detrended) and identified the IMF corresponding to the 11-year cycle using the Lomb-Scargle periodogram<sup>59,60</sup>. As shown by the orange curve in Fig. 3f, the second IMF of the unfiltered dataset exhibits a dominant period of 10.83 years. To estimate uncertainty, we performed Monte Carlo simulations using the measured  $\Delta^{14}\text{C}$  values and their associated uncertainties, and applied EMD to each realization. Interestingly, nearly half of these IMFs exhibit peak-to-peak intervals shorter than 8 years (Fig. 3d), inconsistent with sunspot records. These 5–8 year cycles may represent noise or potentially meaningful solar signals, as similar periodicities have been observed in  $^{10}\text{Be}$  data<sup>61,62</sup> and recent observation of the OSF, representing the solar magnetic flux transported through the heliosphere (see SI, Fig. S15). This suggests possible mode mixing—a known limitation of EMD<sup>58</sup>—between the short-period and 11-year components. To mitigate mode mixing, we applied an 8-year low-pass filter before EMD. The resulting IMF (green curve in Fig. 3b) shows a dominant period of 13.26 years, with peak-to-peak intervals ranging from 7.5 to 16.5 years (Fig. 3d, f). To validate whether the pre-filtered IMF reflects actual solar cycle features, we compared the filtered  $\Delta^{14}\text{C}$  data (1700–1933, from Brehm et al.<sup>15</sup>) with contemporaneous sunspot records (see SI, Fig. S16). While the IMF does not precisely track individual sunspot fluctuations, it reproduces key features such as cycle count and amplitude variation. Note that the pre-filtered IMF is not a direct reconstruction of the 11-year cycle, as EMD is sensitive to the choice of band-pass cutoff frequencies. Finally, we evaluated the statistical significance of the extracted IMFs using the method proposed by Mehta et al.<sup>63</sup>, comparing their energy to a  $\chi^2$ -distributed baseline derived from Monte Carlo simulations of red-noise time series. Both selected IMFs exhibit statistically significant signals (see SI, Figs. S12 and S14).

When examining variations in the 11-year cycle during GSM, we observe patterns of weakening and recovery consistent with previous studies<sup>10,15,19</sup>. As shown in Fig. 3e, Morlet wavelet analysis indicates that the

11-year signal is weak or nearly absent during GSM in both filtered and unfiltered IMFs, consistent with the findings of Brehm et al.<sup>16</sup> for the first millennium BCE. Notably, the pre-filtered IMF reveals two distinct patterns of variation (the zoomed-in view is shown in SI Fig. S18). In relatively short GSM (105–150 CE and 400–450 CE), the amplitude of the 11-year cycle symmetrically weakens and recovers (from around 0.5‰ to exceeding 1‰), accompanied by possible period changes of several years. Note that the period variation could also be the result of EMD mode mixing, as discussed above. In contrast, longer GSM (200–280 CE and 640–730 CE) exhibit a different pattern: the cycle begins with reduced amplitude (around 0.5‰), rebounds to >1‰ mid-period, and then weakens again toward the end. Cycle length variations in these longer GSM also follow a distinct trajectory—initially lengthening from ~10 to ~13 years, then shortening back to ~10 years. This feature of both amplitude and period variation is reminiscent of the Maunder Minimum, as reported by Fogtman-Schulz et al.<sup>19</sup>, which spanned a similar duration (97 years). Moreover, we also analyzed data from Brehm et al. in the last millennium, which shows similar patterns in its four Maunder-type GSM (see SI Fig. S19). Notably, from the direct sunspot observations during the Maunder Minimum, a cycle length of  $13.2 \pm 0.6$  years, if considering only the well-observed cycles, was reported by Vaquero et al.<sup>18</sup>, and it can vary between 9 and 18 years, which is comparable with what is presented in SI Fig. S19d presented. Additionally, Miyahara et al.<sup>23</sup> documented a lengthening of the Schwabe cycle to 16 years across three consecutive cycles before the Maunder Minimum—a pattern not observed in our dataset. In the pre-filtered IMF, the longest of the five cycles preceding each GSM does not exceed 13 years. However, we successfully extracted the 11-year cycle with pre-filtered IMF using  $\Delta^{14}\text{C}$  data for the Maunder minimum measured by Miyahara et al.<sup>23</sup>, which is identical to what they reconstructed with production computation (SI, Fig. S17).

### Spike scan

Annual resolution records of the intermediate-sized Miyake Events are urgently needed. Such data not only help refine the occurrence rate for the SEP hypothesis<sup>35</sup> but also provides statistical information for assessing and mitigating the potential impact of high-energy particle events on modern society<sup>64</sup>. In this study, we applied a Bayesian approach to infer the posterior distribution of the start, duration, and additional  $^{14}\text{C}$  production ( $Q$ ) associated with each annual measurement across all seven composite datasets. A 5-year moving window was applied as the calculation period, with  $Q$  representing the production increase in the central year relative to the preceding years in the same window. From the MCMC simulations, we extracted the stable posterior chain of  $Q$  and derived its empirical distribution. The cumulative probabilities exceeding selected thresholds (e.g.,

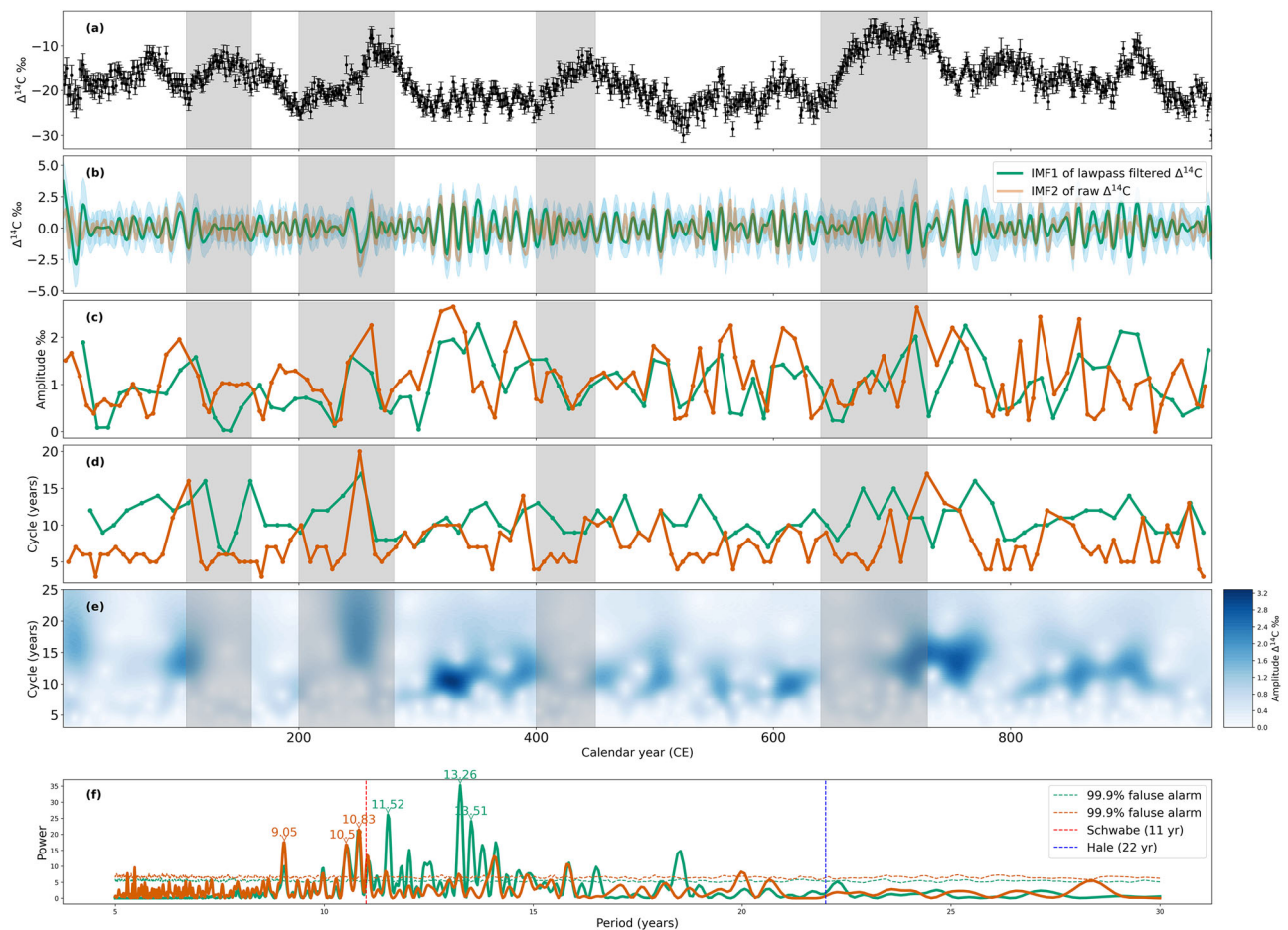


**Fig. 3 | Solar cycle extraction from the single-year  $^{14}\text{C}$  record (1–970 CE) with four candidate GSM indicated in gray.** **a** Single-year  $\Delta^{14}\text{C}$  data from 1–970 CE (775 CE spike detrended), and the error bars indicate the  $\pm 1\sigma$  measurement uncertainties. **b** Two Intrinsic Mode Functions (IMFs) extracted by Empirical Mode Decomposition (EMD) with the uncertain range estimated by Monte Carlo simulation. The green curve corresponds to the IMF extracted from EMD after applying an 8-year low-pass filter applied to the original  $\Delta^{14}\text{C}$  data, and the orange curve corresponds to

the IMF extracted from the original  $\Delta^{14}\text{C}$  data without filtering. **c** 3-year moving average of the amplitude of the extracted IMFs. **d** 3-year moving average of the cycle length (expressed by peak-to-peak distance) for the extracted IMFs. **e** Morlet wavelet spectrum of the extracted IMFs. The color scale from white to blue indicates the strength of the amplitude. **f** Lomb-Scargle spectrum of the extracted IMFs, with the three cycle length with highest power marked and 99.9% false alarm threshold plotted. The extracted IMF predominantly shows an 11-year cycle.

$Q > 3.5$ ,  $Q > 1.5$ ,  $Q > 1$  atom  $\text{cm}^{-2} \text{s}^{-1} \text{yr}^{-1}$ ) were subsequently used as proxies for the probability of a spike. As shown in Fig. 4, the 775 CE spike stands out across the entire range of  $Q$ . To select candidates, we also analyzed two medium-sized events (1052 CE and 1280 CE) from Brehm et al.<sup>15</sup>. The results show approximately a 50% probability that  $Q$  exceeded 1.5 atom  $\text{cm}^{-2} \text{s}^{-1} \text{yr}^{-1}$  during these events (see SI Fig. S21). If we apply this criterion to our datasets, then 14 CE ( $>6\%$  rise), 325 CE ( $>6\%$  rise), 508 CE ( $>5\%$  rise), 553 CE ( $>5\%$  rise), 598 CE ( $>5\%$  rise), 605 CE ( $>8\%$  rise), 675 CE ( $>5\%$  rise), 893 CE ( $>5\%$  rise), and 954 CE ( $>7\%$  rise) can be identified as events of potential interest.

Of these nine possible events, five (325, 508, 598, 605, and 893 CE) are less likely to be SEP events due to either the absence of a globally coherent abrupt rise in  $\Delta^{14}\text{C}$  or the persistence of the increased  $\Delta^{14}\text{C}$  after the rise. Following Zhang et al.<sup>65</sup>, two key indicators for SEP-related  $^{14}\text{C}$  signals are (1) a universal abrupt rise in  $\Delta^{14}\text{C}$  within 1–2 years; and (2) an exponential decline afterwards, reflecting carbon cycle effects. The 325 CE was removed because its rise appears in only one of two overlapping datasets with the other showing a gradual 5‰ rise over 6 years. To exclude short-lived fluctuations further, we evaluated the 3-year average change before and after each rise. As shown in Table 2, the differences for 508, 598, and 893 CE were 2.99‰, 1.73‰, and 1.54‰, respectively - all within the twice measurement uncertainty range ( $\sigma \sim 1.5\%$ ). In contrast, for 14, 553, 605, 675, and 954 CE, the 3-year average increases exceed  $2\sigma$ . Of these, 603 CE displayed a

sustained rise of 2.73‰ per year for three consecutive years (Fig. 5b). Although a similar pattern occurred during the 663 BCE event<sup>28,65</sup>, the rate of change in that case was much faster (up to 5‰ per year). Thus, 603 CE is removed from further consideration. The other three cases all show abrupt increases followed by 2–3 years of elevated  $^{14}\text{C}$  values (Fig. 5a, c, d), suggesting they may be medium-scale Miyake Events, warranting further confirmation from additional tree-ring samples. It is also worth noting that in the annual dataset from Brehm et al.<sup>16</sup>, there is only a 2.3‰ rise between 955 and 956 CE. However, considering the analytical uncertainties of the two years in their data (2.12‰ and 2.14‰) and in this study's measurements (1.36‰ and 1.41‰), we still include it for further verification. It should also be noted that after the 14–15 CE rise ( $>6\%$ ), the  $\Delta^{14}\text{C}$  drops to the level before the rise in the next year, however, it jumps back with another  $>6\%$  rise in 16 CE. Judging from the fluctuations over these three years, the credibility of a spike existing in 14–15 CE is weakened, but from the long-term trend (Fig. 1a and Fig. 5a), the discontinuity of the change is also clear. Thus, verification from other datasets will be necessary to confirm this candidate event.

## Discussion

The analysis of solar activity derived from annual  $^{14}\text{C}$  records in the first millennium CE, ranging from long-term to short-term variations, offers valuable insights into solar dynamo behavior. Our new dataset reveals

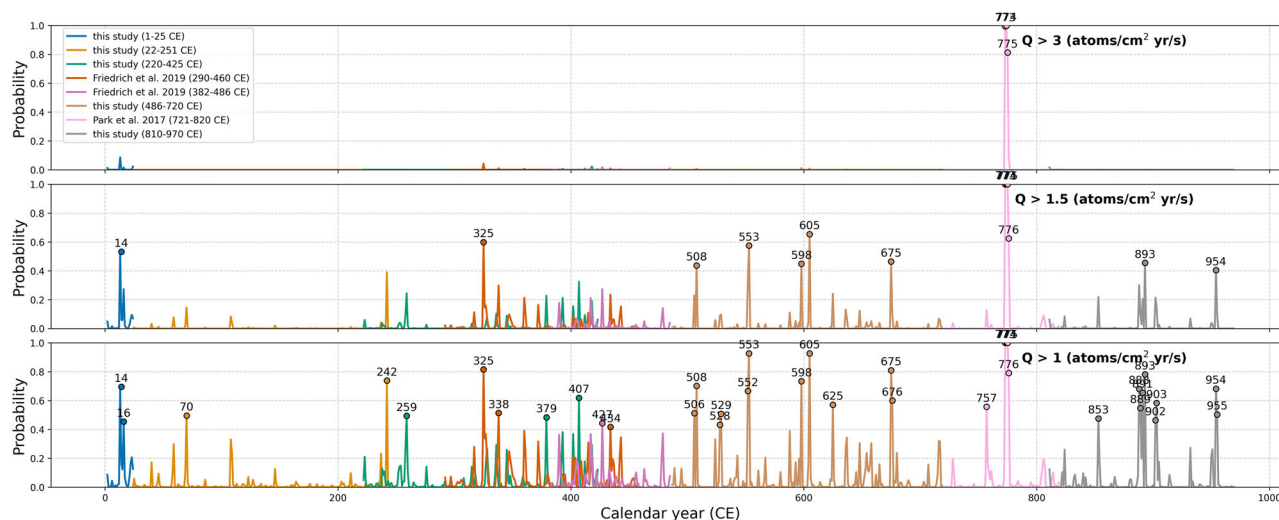


**Fig. 4 | The probability of occurrence of various levels of additional <sup>14</sup>C production (Q) related to a potential spike, based on the seven datasets from 1 to 970 CE. From top to bottom, each panel corresponds to a Q threshold ranging from 1 to 3.5 atom cm<sup>-2</sup> s<sup>-1</sup> yr<sup>-1</sup>. Years with a probability greater than 40% are indicated.**

**Table 2 | 3-year average increase in Δ<sup>14</sup>C before and after each potential spike found in the seven datasets from 1 to 970 CE**

Spike (CE)	3-yr increase (‰)
14	4.78‰
<b>508</b>	<b>2.99‰</b>
553	4.56‰
<b>598</b>	<b>1.73‰</b>
605	3.24‰
675	3.42‰
<b>893</b>	<b>1.54‰</b>
954	3.53‰

Candidates that are within the ±2σ measurement uncertainty range in bold.

several offsets from the IntCal20 curve, which not only affect <sup>14</sup>C dating calibration but also lead to revised estimates of past solar activity. Using a GPR with control points computation scheme, this study reconstructs a statistically robust record of the solar modulation parameter, showing strong agreement with previous reconstructions, but providing much greater detail.

Based on the newly reconstructed record, four GSM were revealed, and, when combined with solar cycle analysis, provided further insights into solar variability. Earlier studies have shown that Schwabe cycles tend to weaken during GSM<sup>15,19,20</sup>. Building on this, we employed EMD with an 8-year low-pass pre-filter to extract 11-year solar cycle signals and identified two patterns of solar cycle variation during the GSM.

The robustness of this method was verified through a Monte Carlo significance test, Lomb-Scargle spectral analysis, and comparison with observed sunspot data. It is worth noting that the unfiltered IMF also exhibits 5-8 year cycles. While their origin remains uncertain, similar periodicities have been reported in other solar proxies, suggesting a potential solar source, though exploring this is beyond the scope of this study.

In the pre-filtered EMD results, two distinct patterns of weakening and recovery during GSM are evident. According to Karak<sup>66</sup>, during Maunder-type GSM, a diffusion-dominated solar dynamo leads to a weaker magnetic field, as the poloidal component dissipates more readily. This results in a reduced Schwabe cycle amplitude. In such regimes, the cycle period is primarily governed by the diffusive timescale, which is generally longer than in advection-dominated regimes-though not always-potentially leading to lengthened solar cycles. This framework may help explain the two longer GSM identified in this study.

In contrast, the shorter GSM (approximately 40 years) shows a more symmetric weakening and recovery in both amplitude and period. Using a model of OSF and <sup>10</sup>Be, Owens et al.<sup>67</sup> showed that when solar activity is low, the OSF becomes more sensitive to the inclination of the heliospheric current sheet rather than the variation of sunspot number. This may account for the symmetric Schwabe cycle behavior observed here.

At shorter timescales, this study also developed a comprehensive method for identifying intermediate Miyake Events (i.e., “spike scan”) and, in so doing, identified four candidates around 14, 553, 675, and 954 CE. According to Usoskin et al.<sup>34</sup>, if these events are indeed SEP-related, they can shed light on their origins and frequency, aiding in the evaluation of related high-energy particle risks. In a recent study, Brehm et al.<sup>16</sup> used a convenient method that compares the 3-year average before and after each year. If the difference exceeds the bounds of a theoretical normal distribution, a potential event is flagged. However, intermediate Miyake Events that produce a 4-5‰ rise can be easily obscured by natural variability and may escape detection with such methods. In this study, we applied a Bayesian approach, using a carbon box model to compute the posterior distribution of the additional <sup>14</sup>C production rate (Q). Nine moderate increases were initially flagged, while none of them could be identified with Brehm’s method (see SI, Fig. S20), and five were later excluded after further analysis. This highlights that while spike scans are useful for initial detection, more rigorous follow-up, such as multi-dataset comparison, mean-shift analysis, and detailed modeling, is essential for confirming candidate events.

Future research should aim to expand the geographic and species coverage of high-resolution <sup>14</sup>C records to test the global synchronicity of solar-induced events. Incorporating additional archives, such as ice cores and <sup>10</sup>Be records, may also enhance the resolution and cross-validation of solar activity reconstructions. With regard to methodology, developing adaptive signal extraction techniques that can account for variability in solar cycle length will improve the detection of subtle dynamo changes during GSM.

## Methods

### Radiocarbon (<sup>14</sup>C) measurement

Tree-ring samples were obtained from oaks collected in Germany and France, mainly from the Hohenheim tree-ring archive<sup>68</sup> curated at Curt-Engelhorn-Centre Archaeometry in Germany, with additional material from the site “Zeven-Wistedt H60 + H72” in northern Germany. Ring widths were measured to 0.01 mm precision and cross-dated against established regional oak chronologies using TsapWin<sup>TM</sup> software. Independent redating at the Hemmenhofen Dendrochronological Laboratory

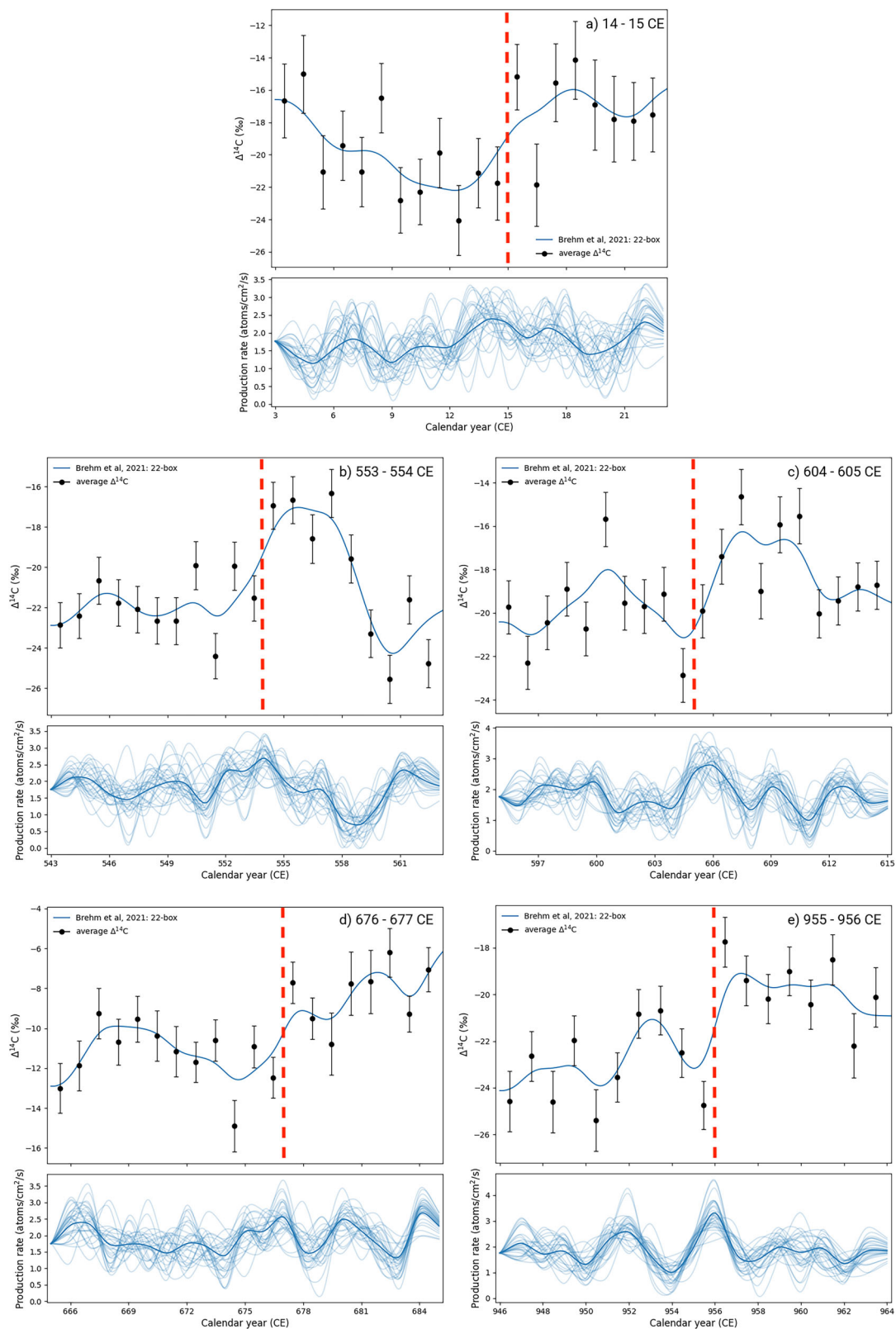


**Fig. 5 | Measured results and calculated <sup>14</sup>C production rates for the five spike candidates. a** 14-15 CE, **(b)** 553-554 CE, **(c)** 604-605 CE, **(d)** 676-677 CE, and **(e)** 955-956 CE. The upper panels in each subplot show the measured  $\Delta^{14}\text{C}$  values with  $\pm 1\sigma$  uncertainties (black dots and error bars) and the best fit from Gaussian Process

Regression (blue lines). The red lines indicate the onset of each rise. The lower panels in each subplot present the Monte Carlo Markov Chain (posterior distribution draw) of production rates and  $\Delta^{14}\text{C}$ , computed using Gaussian Process Regression with control points.

confirmed full agreement between laboratories. Latewood was used for radiocarbon analysis, except for the Zeven-Wistedt samples, which comprised complete rings. Additional tree-ring material (Q9894, 1–25 CE) was provided by Queen’s University Belfast, UK. Details of sample provenance, dendrochronological procedures, and cross-dating results are provided in SI Tables S1–S3.

Tree-ring samples were pretreated and analyzed for radiocarbon analysis at the Curt-Engelhorn-Centre Archaeometry by isolating  $\alpha$ -cellulose. This cellulose fraction is considered the most reliable carbon-bearing component in wood due to its chemical stability and resistance to diagenetic alteration.

The pretreatment followed a standard  $\alpha$ -cellulose extraction protocol. Samples first underwent an acid-base-acid (ABA) sequence consisting of 1.5 M HCl (30 min, 80 °C), 17.5% w/v NaOH (1 h, 80 °C), and a final 1.5 M HCl rinse (30 min, 80 °C), with ultrapure water rinses between each step. Subsequently,  $\alpha$ -cellulose was further purified by treating the sample with a mixture of 1.5% w/v sodium chlorite (NaClO<sub>2</sub>) and HCl until the pH reached 3 at 80 °C for a minimum of 20 hours, followed by thorough rinsing and drying.

The purified  $\alpha$ -cellulose was combusted in an *Elementar VarioMicro* elemental analyzer to produce CO<sub>2</sub>, which was cryogenically trapped and reduced to graphite using either an in-house 10-reactor graphitization system or an automated AGE3 system (Ionplus AG). Graphite targets were pressed into aluminum holders and measured using one of the MICADAS accelerator mass spectrometers (AMS). Each analytical run included international and in-house standards as well as background materials (phthalic anhydride and ancient wood material). Data reduction was performed with the BATS 4.3 software<sup>8</sup> to calculate conventional <sup>14</sup>C ages. A laboratory-specific additional uncertainty (sample scatter) of 0.1% was applied to account for uncertainties that are not covered by purely analytical errors. Additionally, the <sup>14</sup>C laboratory at the University of Groningen carried out fifteen replicate measurements for external verification and sample measurements for 1–25 CE following the  $\alpha$ -cellulose extraction protocol described in Dee et al.<sup>69</sup> Similar to the Curt-Engelhorn-Centre Archaeometry, the CIO also applied an ABA pretreatment followed by NaClO<sub>2</sub> treatment to extract the  $\alpha$ -cellulose, with the base step under ultrasonication and a nitrogen atmosphere. Subsequently, the extracted  $\alpha$ -cellulose was combusted to CO<sub>2</sub> using an elemental analyzer (*Elementar VarioMicro*) and then converted to graphite using an homemade graphitization system. The graphite targets were measured using the MICADAS AMS at the CIO.

Data correction and quality control of the measurement included background subtraction, internal reproducibility tests, and the use of inter-laboratory comparisons. Background values were established using pretreated Kauri wood and xyloid lignite beyond the <sup>14</sup>C dating range, yielding consistent results (mean F<sup>14</sup>C = 0.0028 ± 0.0007). Internal reproducibility was assessed using 28 multi-ring oak samples (“Wetterbrücke”, 1000–1021 CE), showing good consistency ( $\sigma_{F^{14}C} = 0.0022$ ; reduced  $\chi^2 = 1.0$ ). External verification was performed by parallel analyses with the Groningen laboratory on 15 samples (71–116 CE), resulting in an average offset of 4 ± 15 years and no systematic differences between labs. Further details and supporting figures are provided in SI Figs. S1–S4 and Table S4.

### Data merging

To construct the integrated dataset, data from the same year were selected primarily based on the  $\chi^2$  test, followed by a detailed cross-comparison with adjacent years. For years with multiple measurements, the Ward & Wilson  $\chi^2$  test, commonly used in the radiocarbon (<sup>14</sup>C) field, was first applied. If the data passed the test, they were merged using the weighted mean:

$$\Delta^{14}C_{\text{merge}} = \frac{\sum_{i=1}^N \Delta^{14}C_i / \sigma_i^2}{\sum_{i=1}^N 1 / \sigma_i^2} \quad (1)$$

$$\sigma_{\text{merge}} = \sqrt{\frac{1}{\sum_{i=1}^N 1 / \sigma_i^2}} \quad (2)$$

where  $n$  is the number of results for that year,  $\Delta^{14}C_i$  is the individual measurement, and  $\sigma_i$  is its uncertainty.

If the data failed the  $\chi^2$  test, an outlier check was performed. For years with more than two values, each point was excluded in turn, and the  $\chi^2$ -test was applied to the remaining data to identify outliers. If only two values were available, and neighboring-year data showed limited variation, the test was repeated using neighboring data in a similar exclusion-based approach. Data that passed after outlier removal were merged using the same weighted formula. For 11 years out of the total 264  $\chi^2$  tests being applied, where no clear outlier was identified but the data still failed the  $\chi^2$ -test, measurement uncertainties were increased until the test was passed (see SI, Table S5)

### Production rate computing with parametric Gaussian Process Regression

Prior to solar activity reconstruction, <sup>14</sup>C production rate needs to be first computed from the measured  $\Delta^{14}C$  results. It is typically done with carbon box modeling<sup>15,52,70,71</sup>. Carbon box modeling simplifies the global carbon cycle by dividing the Earth system into a limited number of interconnected reservoirs-called boxes-such as the stratosphere, troposphere, terrestrial biosphere, and different ocean layers. Each box is assumed to be internally well-mixed and spatially homogeneous, so carbon within a box can be represented by a single mass or concentration value. Carbon exchange between boxes is represented by prescribed flux rates, typically based on steady-state observations. The model assumes that carbon fluxes change proportionally with deviations from steady-state reservoir sizes, and that isotopic ratios (e.g., <sup>14</sup>C/<sup>12</sup>C) are transported without fractionation unless otherwise specified.

The time evolution of carbon in each box is described using mass-balance differential equations that account for carbon inputs, outputs, radioactive decay (for <sup>14</sup>C), and production processes. The system is solved numerically with small time steps (monthly) to track how changes propagate through the carbon cycle. Observed atmospheric radiocarbon variations from tree rings can then be used to invert the model and reconstruct past changes in <sup>14</sup>C production or solar activity.

In carbon box modeling, one persistent challenge lies in handling the uncertainty introduced by deterministic inverse solvers of ordinary differential equations governing the carbon cycle. As shown by Zhang and colleagues<sup>65</sup>, such solvers tend to amplify short-term noise, leading to unrealistic variability in the inferred production rates. To mitigate this, Miyake et al.<sup>52</sup> introduced 1,000 random realizations of  $\Delta^{14}C$  measurement uncertainty, yet still observed an average error of ~1 atom cm<sup>-2</sup> s<sup>-1</sup> yr<sup>-1</sup>-over 30% of the estimated production rate. On longer, millennial timescales, Brehm et al.<sup>15,16</sup> applied a Savitzky-Golay filter alongside Monte Carlo sampling to constrain production rates within measurement uncertainty bounds. While this approach reduces noise, applying a separate filter in each Monte Carlo iteration risks incorporating the filter’s own variability into the final uncertainty. If the filter suppresses true signals or amplifies noise, it can distort the inferred uncertainty range, conflating measurement error with artifacts introduced by the filtering process.

To obtain accurate estimates with statistically robust uncertainty, we applied a different approach: parametric GPR with control points combined with MCMC for modeling the <sup>14</sup>C production rate. In this method, a set of unknown production rates  $q_i$  is assigned as parameters to each year. These are then interpolated into a continuous function  $\mathbf{q}(t)$  using GPR, which enforces temporal smoothness through a kernel-based covariance structure. The best-fitting parameters are first determined by maximizing (minimizing) the joint log-likelihood:

$$\mathcal{L}(\mathbf{q}) = -\log P(\text{data}) - \log P_{\text{GP}}(\mathbf{q}) \quad (3)$$

where

$$-\log P(\text{data}) = \frac{1}{2} \sum_i \left( \frac{d_i - \hat{d}_i(\mathbf{q})}{\sigma_i} \right)^2 \quad (4)$$

$$-\log P_{\text{GP}}(\mathbf{q}) = \frac{1}{2} \mathbf{q}^T \mathbf{K}^{-1} \mathbf{q} + \frac{1}{2} \log |\mathbf{K}| \quad (5)$$

Here,  $\mathbf{q}$  is the vector of production rate parameters,  $\hat{d}_i(\mathbf{q})$  is the simulated  $\Delta^{14}\text{C}$  from the carbon box model,  $d_i$  is the observed  $\Delta^{14}\text{C}$ ,  $\sigma_i$  is the measurement uncertainty, and  $\mathbf{K}$  is the GPR kernel covariance matrix. This optimized  $\mathbf{q}$  is then used to initialize a Bayesian inference process via MCMC sampling:

$$q^{(i)} \sim P(\mathbf{q} | \text{data}) \propto P(\text{data} | \mathbf{q}) \cdot P_{\text{GP}}(\mathbf{q}) \quad (6)$$

This hybrid method combines the efficiency of optimization with the rigour of Bayesian uncertainty quantification. It produces a full posterior distribution of the production rate at annual resolution, accounting for measurement uncertainty, natural variability (via the GPR kernel), and carbon cycle dynamics. The method is implemented in the open-source package *ticktack*<sup>72</sup> and is compatible with several major carbon box models<sup>15,70,71</sup>. After parameter testing (see SI, Figs. S7, S8, and S9), we selected the Matérn-3/2 kernel function with annual control points (both spacing factor  $\tau$  and length scale  $l$  equal to 1, as shown below), using Brehm et al.<sup>15</sup>'s carbon box model:

$$k_{\text{Matérn-3/2}}(\tau) = \left( 1 + \frac{\sqrt{3}\tau}{l} \right) \exp\left( -\frac{\sqrt{3}\tau}{l} \right) \quad (7)$$

The computation scheme of Gaussian Regression (GP) algorithm with control points in *ticktack* is shown in SI, Fig. S6. To address the  $O(N^3)$  computational cost of GPR, we divided the dataset into five 220-year segments (with 20-year overlaps to mitigate boundary effects by averaging the results) for parallel computation. For more information on this method, please refer to the review of Aigrain and Foreman-Mackey, and the study of Zhang and colleagues<sup>65,73</sup>.

### Detrending the 775 Miyake event

With the abrupt rise in  $\Delta^{14}\text{C}$  during 774-775 CE, the reconstruction of solar activity was strongly affected. This issue has previously been identified with the 663 BCE rise<sup>16</sup>. Importantly, if these were SEP events originating from the Sun, they should be removed from the computation of the solar modulation parameter. This is because SEPs are triggered by very short-term phenomena, solar flares and coronal mass ejections, which are not directly related to sunspot activity and long-term solar magnetic activities<sup>34</sup>. In this study, a  $\Delta^{14}\text{C}$  curve was first constructed using GPR control points for the intervals before and after the 775 CE event (749-775 CE and 791-820 CE) to approximate conditions without the spike. Subsequently, another  $\Delta^{14}\text{C}$  trend was computed using the data from the 775-820 CE interval with the same GPR control points method. By subtracting these two trends and applying the difference to each measurement from 775-791 CE, the long-term trend was removed while short-term fluctuations in the data were retained (see SI, Fig. S5).

### Solar modulation reconstruction

To reconstruct solar activity from the computed  $^{14}\text{C}$  production rates, we employed a well-established framework that links the solar modulation parameter ( $\Phi$ ) to cosmogenic isotope production.  $^{14}\text{C}$  production rates are known to depend on the incident galactic cosmic rays, which are modulated by both solar magnetic activity and geomagnetic field strength. Moreover, the relationship between the solar modulation parameter ( $\Phi$ ), geomagnetic field strength, and cosmogenic isotope (CI) production has been established in several models<sup>43-45</sup> and is applied here. The modeling begins with the Local Interstellar Spectrum (LIS) of GCR, derived from observational

data<sup>43-45</sup>. Using the force-field approximation<sup>74</sup>, which incorporates  $\Phi$ , and applying cut-off energy thresholds based on geomagnetic strength (expressed as the virtual axial dipole moment, VADM, as shown in SI, Fig. S10), the GCR spectrum reaching Earth's atmosphere is determined. The CI production rate is then calculated using relevant CI nuclear reaction cross-sections. This framework allows mapping from a given production rate and VADM to the corresponding  $\Phi$  value.

In this study, the mapping relation by Kovaltsov et al.<sup>44</sup> was adopted as well as the VADM record provided by Panovska et al.<sup>46</sup>. By inserting the computed production rate distribution and VADM records from 1 to 970 CE into the mapping relation, the distribution of  $\Phi$  in each year for the same period was obtained. The resulting  $\Phi$  values show good agreement with those calculated by Wu et al.<sup>47</sup>.

### Identifying the solar cycle with empirical mode decomposition

For solar cycle identification, we applied the EMD instead of a bandpass filter to extract the intrinsic oscillatory components from the  $^{14}\text{C}$  record. Empirical Mode Decomposition, first introduced by Huang et al.<sup>58</sup>, is well-suited for analyzing non-stationary and non-linearly varying signals, a key characteristic of solar cycles. It has previously been used to identify the 11-year solar cycle in stratospheric ozone signals<sup>75</sup>. The EMD algorithm first identifies all local maxima and minima of the signal and interpolates them using cubic splines to form the upper and lower envelopes, denoted as  $e_{\text{max}}(t)$  and  $e_{\text{min}}(t)$ , respectively.

The local mean of the signal is then computed as

$$m(t) = \frac{e_{\text{max}}(t) + e_{\text{min}}(t)}{2} \quad (8)$$

Subtracting this mean from the signal yields a proto-Intrinsic Mode Function (IMF):

$$h(t) = x(t) - m(t). \quad (9)$$

This sifting process—removing the mean and checking whether the component meets the criteria—is repeated until  $h(t)$  satisfies the IMF definition: (1) The numbers of extrema and zero-crossings differ at most by one. (2) The mean of the upper and lower envelopes is approximately zero:

$$\frac{1}{T} \int_0^T h(t) dt \approx 0. \quad (10)$$

when the above conditions are satisfied,  $h(t)$  is considered an extracted IMF:

$$\text{IMF}_1(t) = h(t). \quad (11)$$

Once an IMF is extracted, it is removed from the original signal:

$$r_1(t) = x(t) - \text{IMF}_1(t), \quad (12)$$

and the sifting procedure is applied to the residual  $r_1(t)$  to extract the next IMF. The iteration continues until the residual becomes a monotonic function. The original signal can then be represented as

$$x(t) = \sum_{i=1}^N \text{IMF}_i(t) + r_N(t), \quad (13)$$

where  $x(t)$  denotes the original signal,  $\text{IMF}_i(t)$  are the Intrinsic Mode Functions, and  $r_N(t)$  is the monotone residual component.

In real application, this study used the open-source Python package *PyEMD* and implement the Complete Ensemble Empirical Mode Decomposition with Adaptive Noise (CEEMDAN), which is an enhanced version of EMD designed to overcome mode mixing and IMF inconsistencies observed in classical EMD. CEEMDAN introduces adaptive noise-assisted decomposition while guaranteeing that each IMF is unique and stable. The

key principle is to iteratively add averaged noise IMFs into the residual signal decomposition stage. This ensures that the statistical characteristics of noise aid decomposition without contaminating the final IMFs.

Let the original signal be  $x(t)$ , and let  $w_k(t)$  be independent realizations of white noise, with  $K$  ensemble trials.

### 1. Extract the First IMF

Add white noise to the signal:

$$x_k(t) = x(t) + \varepsilon_0 w_k(t), \quad (14)$$

Apply EMD to obtain the first IMF:

$$c_{1,k}(t) = \text{IMF}_1(x_k(t)), \quad (15)$$

Compute the ensemble average:

$$c_1(t) = \frac{1}{K} \sum_{k=1}^K c_{1,k}(t), \quad (16)$$

Obtain the first residual:

$$r_1(t) = x(t) - c_1(t). \quad (17)$$

### 2. Extract the Second IMF

Compute the averaged first IMF of the white noise:

$$\overline{w_1(t)} = \frac{1}{K} \sum_{k=1}^K \text{IMF}_1(w_k(t)). \quad (18)$$

Add this adaptive noise component to the residual:

$$r_1(t) + \varepsilon_1 \overline{w_1(t)}, \quad (19)$$

Apply EMD again to obtain:

$$c_2(t) = \text{IMF}_2(r_1(t) + \varepsilon_1 \overline{w_1(t)}), \quad (20)$$

Update the residual:

$$r_2(t) = r_1(t) - c_2(t). \quad (21)$$

### 3. General Iterative Step

At the  $n$ -th step, obtain the IMF as:

$$c_n(t) = \text{IMF}_n(r_{n-1}(t) + \varepsilon_{n-1} \cdot \overline{\text{IMF}_{n-1}(w(t))}), \quad (22)$$

Update the residual iteratively:

$$r_n(t) = r_{n-1}(t) - c_n(t). \quad (23)$$

Continue this process until  $r_n(t)$  becomes a monotonic component from which no further IMF can be extracted. The final residual is considered the trend of the original signal.

To estimate the uncertainty of the extracted IMFs, we performed Monte Carlo simulations by randomly sampling the measured  $\Delta^{14}\text{C}$  values within their uncertainties and applying CEEMDAN to each realization. The resulting distribution of IMFs was then used to compute the mean and standard deviation of each IMF, providing a robust estimate of uncertainty. The statistical significance of each IMF was assessed by comparing its energy to a  $\chi^2$  distribution fitted to the energies of IMFs derived from Monte Carlo simulations of red-noise time series, following the approach of Mehta et al.<sup>63</sup>. This allows identification of IMFs whose energies exceed the 95% significant threshold, indicating they likely

represent real signals rather than noise (see SI, Figs. S11, S12, S13, and S14). To further resolve periodic components within the extracted IMFs, we applied Lomb-Scargle spectral analysis<sup>59,60</sup>. At each trial frequency, this method adjusts for irregular sampling by shifting the phases to maximize the fit of a sinusoidal curve to the data. The resulting power spectrum highlights dominant periodic components, regardless of gaps or irregularities in the time series. Based on the Lomb-Scargle spectrum, we identified IMFs corresponding to the 11-year solar cycle. The above protocol was also implemented on an 8-year low-pass filtered  $\Delta^{14}\text{C}$  record to mitigate mode mixing between the 11-year cycle and shorter periodicities (5–8 years) that may arise from noise or other solar signals. Combined with GSM candidates from solar activity reconstruction, we then examined the behavior, in terms of cycle length and amplitude, of the 11-year cycle.

### Bayesian approach for spike scan

A primary purpose of single-year measurements is to identify abrupt increases, or “spikes”, which may be associated with SEP events. Using a Bayesian MCMC approach, we iterated through every year in each individual dataset within the millennia-long record to comprehensively search for such signals. Our approach is similar to that of Gütler et al.<sup>71</sup>, who tested different production magnitudes, durations, and timings within a carbon box model to find the best match (using least squares) to the measured  $\Delta^{14}\text{C}$ . However, in this study, we specified the duration (within 1 year) and timing (center of the moving window) of  $^{14}\text{C}$  production in a moving window of 5- and 11-year lengths. This information was incorporated as a prior in the Bayesian framework. Subsequently, an MCMC simulation was performed in *ticktack*, using the carbon box model, to produce the posterior distributions of the magnitude (additional production rate), start, and duration for each moving window. By running the calculation for each year (taking it as the centered year of the moving window), we obtained the posterior distribution of the corresponding additional  $^{14}\text{C}$  production rate (Q). Subsequently, we calculated the cumulative probability of Q exceeding certain thresholds (from 1 to 3.5 atom  $\text{cm}^{-2} \text{s}^{-1} \text{yr}^{-1}$  with a step of 0.5 atom  $\text{cm}^{-2} \text{s}^{-1} \text{yr}^{-1}$ ) for each year. This provides a probabilistic assessment of potential spike events across the entire time series. An advantage of this method is that it quantifies both the probability and the strength of a potential event. After comparing different window sizes, the 5-year window was selected, as it was less affected by the Schwabe cycle (results for the 11-year window are shown in SI, Fig. S22).

### Reporting summary

Further information on research design is available in the Nature Portfolio Reporting Summary linked to this article.

### Data availability

All  $\Delta^{14}\text{C}$  datasets used in this study, including the newly measured data with corresponding tree-ring information and the previously published datasets, are provided in the accompanying zip file (Supplementary Data 1) and have also been deposited on GitHub (<https://github.com/jianwang-rug/HISCAR.git>). Other computed data, including the reconstructed solar modulation parameter values, Bayesian modeling results, and EMD intermediate data, are also included in the GitHub repository.

### Code availability

The code for all analysis methods applied in this study, including data merging, production rate computation, solar modulation reconstruction, EMD analysis, and spike scan, is hosted on GitHub (<https://github.com/jianwang-rug/HISCAR.git>). Customized modifications to *ticktack* for the current study is available upon request, please contact J.W. ([jian.wang@rug.nl](mailto:jian.wang@rug.nl)).

Received: 26 August 2025; Accepted: 9 December 2025;  
Published online: 06 January 2026

## References

- Grieder, P. K. F. *Cosmic Rays at Earth: Researcher's Reference, Manual and Data Book* (Elsevier Science Ltd, 2001).
- Bronk Ramsey, C. Radiocarbon dating: revolutions in understanding. *Archaeometry* **50**, 249–275 (2008).
- de Vries, H. *Variation in Concentration of Radiocarbon with Time and Location on Earth* (Akademie Van Wet, 1958). <https://books.google.nl/books?id=kfbgSAAACAAJ>.
- Stuiver, M. Variations in radiocarbon concentration and sunspot activity. *J. Geophys. Res.* **66**, 273–276 (1961).
- Suess, H. E. The radiocarbon record in tree rings of the last 8000 years. *Radiocarbon* **22**, 200–209 (1980).
- Povinec, P., Burchuladze, A. A. & Pagava, S. V. Short-term variations in radiocarbon concentration with the 11-year solar cycle. *Radiocarbon* **25**, 259–266 (1983).
- Synal, H. A., Stocker, M. & Suter, M. Micadas: a new compact radiocarbon AMS system. *Nucl. Instrum. Methods Phys. Res. Sect. B: Beam Interact. Mater. At.* **259**, 7–13 (2007).
- Wacker, L. et al. Micadas: routine and high-precision radiocarbon dating. *Radiocarbon* **52**, 252–262 (2010).
- Friedrich, R. et al. Annual  $^{14}\text{C}$  tree-ring data around 400 AD: Mid- and high-latitude records. *Radiocarbon* **61**, 1305–1316 (2019).
- Kaiser Kudsk, S. G. et al. Solar variability between 650 CE and 1900-novel insights from a global compilation of new and existing high-resolution  $^{14}\text{C}$  records. *Quat. Sci. Rev.* **292**, 107617 (2022).
- Park, J., Southon, J., Fahrni, S., Creasman, P. P. & Mewaldt, R. Relationship between solar activity and  $\Delta^{14}\text{C}$  peaks in AD 775, AD 994, and 660 BC. *Radiocarbon* **59**, 1147–1156 (2017).
- Eastoe, C. J., Tucek, C. S. & Touchan, R.  $\Delta^{14}\text{C}$  and  $\delta^{13}\text{C}$  in annual tree-ring samples from sequoiadendron giganteum, AD 998–1510: Solar cycles and climate. *Radiocarbon* **61**, 661–680 (2019).
- Fahrni, S. M. et al. Single-Year German oak and Californian Bristlecone Pine  $^{14}\text{C}$  data at the beginning of the Hallstatt Plateau from 856 BC to 626 BC. *Radiocarbon* **62**, 919–937 (2020).
- Land, A., Kromer, B., Remmele, S., Brehm, N. & Wacker, L. Complex imprint of solar variability on tree rings. *Environ. Res. Commun.* **2**, 101003 (2020).
- Brehm, N. et al. Eleven-year solar cycles over the last millennium revealed by radiocarbon in tree rings. *Nat. Geosci.* **14**, 10–15 (2021).
- Brehm, N. et al. Tracing ancient solar cycles with tree rings and radiocarbon in the first millennium BCE. *Nat. Commun.* **16**, 406 (2025).
- Usoskin, I. G., Mursula, K. & Kovaltsov, G. A. Heliospheric modulation of cosmic rays and solar activity during the Maunder minimum. *J. Geophys. Res.: Space Phys.* **106**, 16039–16046 (2001).
- Vaquero, J. M., Kovaltsov, G. A., Usoskin, I. G., Carrasco, V. M. S. & Gallego, M. C. Level and length of cyclic solar activity during the Maunder minimum as deduced from the active-day statistics. *Astron. Astrophys.* **577**, A71 (2015).
- Fogtmann-Schulz, A. et al. Variations in solar activity across the spörer minimum based on radiocarbon in Danish oak. *Geophys. Res. Lett.* **46**, 8617–8623 (2019).
- Inceoglu, F. Exploring solar dynamo behavior using an annually resolved carbon-14 compilation during multiple grand solar minima. *Sci. Rep.* **14**, 5617 (2024).
- Inceoglu, F., Arlt, R. & Rempel, M. The nature of grand minima and maxima from fully nonlinear flux transport dynamos. *Astrophys. J.* **848**, 93 (2017).
- Suess, H. E. Radiocarbon concentration in modern wood. *Science* **122**, 415–417 (1955).
- Miyahara, H. et al. Gradual onset of the Maunder Minimum revealed by high-precision carbon-14 analyses. *Sci. Rep.* **11**, 5482 (2021).
- Usoskin, I. G. et al. Solar cyclic activity over the last millennium reconstructed from annual  $^{14}\text{C}$  data. *Astron. Astrophys.* **649**, A141 (2021).
- Usoskin, I. et al. Sunspot cycles for the first millennium BC reconstructed from radiocarbon. *Astron. Astrophys.* **698**, A182 (2025).
- Miyake, F., Nagaya, K., Masuda, K. & Nakamura, T. A signature of cosmic-ray increase in AD 774–775 from tree rings in Japan. *Nature* **486**, 240–242 (2012).
- Miyake, F., Masuda, K. & Nakamura, T. Another rapid event in the carbon-14 content of tree rings. *Nat. Commun.* **4**, 1748 (2013).
- O'Hare, P. et al. Multiradionuclide evidence for an extreme solar proton event around 2,610 B.P. (~660 BC). *Proc. Natl Acad. Sci.* **116**, 5961–5966 (2019).
- Brehm, N. et al. Tree-rings reveal two strong solar proton events in 7176 and 5259 BCE. *Nat. Commun.* **13**, 1196 (2022).
- Bard, E. et al. A radiocarbon spike at 14 300 cal yr BP in subfossil trees provides the impulse response function of the global carbon cycle during the late glacial. *Philos. Trans. R. Soc. A: Math., Phys. Eng. Sci.* **381**, 20220206 (2023).
- Koldobskiy, S., Mekhaldi, F., Kovaltsov, G. & Usoskin, I. Multiproxy reconstructions of integral energy spectra for extreme solar particle events of 7176 BCE, 660 BCE, 775 CE, and 994 CE. *J. Geophys. Res.: Space Phys.* **128**, e2022JA031186 (2023).
- Paleari, C. I. et al. Cosmogenic radionuclides reveal an extreme solar particle storm near a solar minimum 9125 years BP. *Nat. Commun.* **13**, 214 (2022).
- Cliver, E. W., Schrijver, C. J., Shibata, K. & Usoskin, I. G. Extreme solar events. *Living Rev. Sol. Phys.* **19**, 1–122 (2022).
- Usoskin, I. et al. Extreme solar events: setting up a paradigm. *Space Sci. Rev.* **219**, 73 (2023).
- Usoskin, I. G. & Kovaltsov, G. A. Mind the gap: New precise  $^{14}\text{C}$  data indicate the nature of extreme solar particle events. *Geophys. Res. Lett.* **48**, e2021GL094848 (2021).
- Miyahara, H. et al. Recurrent large-scale solar proton events before the onset of the Wolf Grand Solar Minimum. *Geophys. Res. Lett.* **49**, e2021GL097201 (2022).
- Miyake, F. et al. A single-year cosmic ray event at 5410 BCE registered in  $^{14}\text{C}$  of tree rings. *Geophys. Res. Lett.* **48**, e2021GL093419 (2021).
- Scifo, A. et al. New data fails to replicate the small-scale radiocarbon anomalies in the early second millennium CE. *Radiocarbon* **66**, 518–531 (2024).
- Usoskin, I. G. et al. Revisited reference solar proton event of 23 February 1956: Assessment of the cosmogenic-isotope method sensitivity to extreme solar events. *J. Geophys. Res.: Space Phys.* **125**, e2020JA027921 (2020).
- Kromer, B., Lindauer, S., Synal, H.-A. & Wacker, L. MAMS—a new AMS facility at the curt-engelhorn-centre for archaeometry, mannheim, germany. *Nucl. Instrum. Methods Phys. Res. Sect. B: Beam Interact. Mater. At.* **294**, 11–13 (2013).
- Aerts-Bijma, A. T., Paul, D., Dee, M. W., Palstra, S. W. L. & Meijer, H. A. J. An independent assessment of uncertainty for radiocarbon analysis with the new generation high-yield accelerator mass spectrometers. *Radiocarbon* **63**, 1–22 (2021).
- Reimer, P. J. et al. The IntCal20 northern hemisphere radiocarbon age calibration curve (0–55 cal kBP). *Radiocarbon* **62**, 725–757 (2020).
- Herbst, K., Muscheler, R. & Heber, B. The new local interstellar spectra and their influence on the production rates of the cosmogenic radionuclides  $^{10}\text{Be}$  and  $^{14}\text{C}$ . *J. Geophys. Res.: Space Phys.* **122**, 23–34 (2017).
- Kovaltsov, G. A., Mishev, A. & Usoskin, I. G. A new model of cosmogenic production of radiocarbon  $^{14}\text{C}$  in the atmosphere. *Earth Planet. Sci. Lett.* **337–338**, 114–120 (2012).
- Poluianov, S. V., Kovaltsov, G. A., Mishev, A. L. & Usoskin, I. G. Production of cosmogenic isotopes  $^7\text{Be}$ ,  $^{10}\text{Be}$ ,  $^{14}\text{C}$ ,  $^{22}\text{Na}$ , and  $^{36}\text{Cl}$  in the atmosphere: Altitudinal profiles of yield functions. *J. Geophys. Res.: Atmos.* **121**, 8125–8136 (2016).

46. Panovska, S., Constable, C. G. & Korte, M. Extending global continuous geomagnetic field reconstructions on timescales beyond human civilization. *Geochem. Geophys. Geosyst.* **19**, 4757–4772 (2018).
47. Wu, C. J. et al. Solar activity over nine millennia: a consistent multi-proxy reconstruction. *Astron. Astrophys.* **615**, A93 (2018).
48. Reimer, P. J. et al. IntCal13 and Marine13 radiocarbon age calibration curves 0–50,000 years cal BP. *Radiocarbon* **55**, 1869–1887 (2013).
49. Eddy, J. A. Case of missing sunspots. *Sci. Am.* **236**, 80–88 (1977).
50. Usoskin, I. G., Solanki, S. K. & Kovaltsov, G. A. Grand minima and maxima of solar activity: new observational constraints. *Astron. Astrophys.* **471**, 301–309 (2007).
51. Inceoglu, F. et al. Grand solar minima and maxima deduced from 10be and 14c: magnetic dynamo configuration and polarity reversal. *Astron. Astrophys.* **577**, A20 (2015).
52. Miyake, F. et al. Large <sup>14</sup>C excursion in 5480 BC indicates an abnormal sun in the mid-holocene. *Proc. Natl Acad. Sci.* **114**, 881–884 (2017).
53. Biswas, A., Karak, B. B., Usoskin, I. & Weisshaar, E. Long-term modulation of solar cycles. *Space Sci. Rev.* **219**, 1–28 (2023).
54. Lassen, K. & Friis-Christensen, E. Variability of the solar cycle length during the past five centuries and the apparent association with terrestrial climate. *J. Atmos. Terrestrial Phys.* **57**, 835–845 (1995).
55. van Driel-Gesztelyi, L. & Owens, M. J. Solar cycle. *Oxford Research Encyclopedia of Physics* (2020). <https://oxfordre.com/physics/view/10.1093/acrefore/9780190871994.001.0001/acrefore-9780190871994-e-9>.
56. Choudhuri, A. R. & Karak, B. B. Origin of grand minima in sunspot cycles. *Phys. Rev. Lett.* **109**, 171103 (2012).
57. Solanki, S. K., Krivova, N. A., Schüssler, M. & Fligge, M. Search for a relationship between solar cycle amplitude and length. *Astron. Astrophys.* **396**, L31–L34 (2002).
58. Huang, N. E. et al. The empirical mode decomposition and the Hilbert spectrum for nonlinear and non-stationary time series analysis. *Proc. R. Soc. Lond. Ser. A: Math. Phys. Eng. Sci.* **454**, 903–995 (1998).
59. Lomb, N. R. Least-squares frequency analysis of unequally spaced data. *Astrophys. Space Sci.* **39**, 447–462 (1976).
60. Scargle, J. D. Studies in astronomical time series analysis. ii. statistical aspects of spectral analysis of unevenly spaced data. *Astrophys. J.* **263**, 835–853 (1982).
61. McCracken, K. G., Beer, J. & McDonald, F. B. A five-year variability in the modulation of the galactic cosmic radiation over epochs of low solar activity. *Geophys. Res. Lett.* **29**, 14–1–14–4 (2002).
62. Usoskin, I. G., Solanki, S. K., Kovaltsov, G. A., Beer, J. & Kromer, B. Solar proton events in cosmogenic isotope data. *Geophys. Res. Lett.* **33**, L08107 (2006).
63. Mehta, T. et al. Cycle dependence of a quasi-biennial variability in the solar interior. *Mon. Not. R. Astron. Soc.* **515**, 2415–2429 (2022).
64. Miyake, F., Usoskin, I. & Poluianov, S. *Extreme Solar Particle Storms: The Hostile Sun* (Institute of Physics Publishing, 2019).
65. Zhang, Q. et al. Modelling cosmic radiation events in the tree-ring radiocarbon record. *Proc. R. Soc. A: Math. Phys. Eng. Sci.* **478**, 20220497 (2022).
66. Karak, B. B. Importance of meridional circulation in flux transport dynamo: the possibility of a Maunder-like grand minimum. *Astrophys. J.* **724**, 1021 (2010).
67. Owens, M. J., Usoskin, I. & Lockwood, M. Heliospheric modulation of galactic cosmic rays during grand solar minima: past and future variations. *Geophys. Res. Lett.* **39**, L19102 (2012).
68. Friedrich, M. et al. The 12,460-Year Hohenheim oak and pine tree-ring chronology from Central Europe—a unique annual record for radiocarbon calibration and paleoenvironment reconstructions. *Radiocarbon* **46**, 1111–1122 (2004).
69. Dee, M. W. et al. Radiocarbon dating at Groningen: new and updated chemical pretreatment procedures. *Radiocarbon* **62**, 63–74 (2020).
70. Büntgen, U. et al. Tree rings reveal globally coherent signature of cosmogenic radiocarbon events in 774 and 993 CE. *Nat. Commun.* **9**, 1–7 (2018).
71. Güttler, D. et al. Rapid increase in cosmogenic <sup>14</sup>C in AD 775 measured in New Zealand kauri trees indicates short-lived increase in <sup>14</sup>C production spanning both hemispheres. *Earth Planet. Sci. Lett.* **411**, 290–297 (2015).
72. Sharma, U., Zhang, Q., Dennis, J. & Pope, B. J. S. ticktack: a Python package for carbon boxmodelling. *J. Open Source Softw.* **8**, 5084 (2023).
73. Aigrain, S. & Foreman-Mackey, D. Gaussian process regression for astronomical time series. *Annu. Rev. Astron. Astrophys.* **61**, 329–371 (2023).
74. Moraal, H. Cosmic-ray modulation equations. *Space Sci. Rev.* **176**, 299–319 (2013).
75. Coughlin, K. T. & Tung, K. K. 11-year solar cycle in the stratosphere extracted by the empirical mode decomposition method. *Adv. Space Res.* **34**, 323–329 (2004).

## Acknowledgements

The study is funded by the research program “Internationale Spitzenforschung” of the Baden-Württemberg Foundation. Thanks to Oliver Neller for cross-checking the dendro-dates. Thanks to the teams of the <sup>14</sup>C laboratories for their excellent work and valuable contributions to the quality of the data. Thanks to Claudia Melisch (Melisch Archäologie KG) and Karl-Uwe Heussner (Dendrochronological laboratory of the DAI Berlin, Germany) for the explicit permission to perform <sup>14</sup>C analysis and for providing the wood material of “Zeven-Wistedt H60 + H72” We also thank the China Scholarship Council (CSC) for their support on this study.

## Author contributions

R.F. and M.D. conceived the study. H.K., T.W., and K.S. were responsible for all the dendrochronology analysis. S.L. performed cellulose extraction. R.F. performed the <sup>14</sup>C measurements, data evaluation and quality control. D.B. provided tree-ring samples for the missing years. B.P. and M.O. provided guidance on solar physics and statistics and reviewed the *ticktack* coding. J.W. was in charge of all the analysis, measurement of part of missing years. And all authors wrote/edited the manuscript.

## Competing interests

The authors declare no competing interests.

## Additional information

**Supplementary information** The online version contains supplementary material available at <https://doi.org/10.1038/s43247-025-03120-4>.

**Correspondence** and requests for materials should be addressed to Jian Wang or Ronny Friedrich.

**Peer review information** *Communications Earth and Environment* thanks Nicolas Brehm and the other, anonymous, reviewer(s) for their contribution to the peer review of this work. Primary Handling Editors: Feifei Zhang and Alireza Bahadori. A peer review file is available.

**Reprints and permissions information** is available at <http://www.nature.com/reprints>

**Publisher’s note** Springer Nature remains neutral with regard to jurisdictional claims in published maps and institutional affiliations.

**Open Access** This article is licensed under a Creative Commons Attribution 4.0 International License, which permits use, sharing, adaptation, distribution and reproduction in any medium or format, as long as you give appropriate credit to the original author(s) and the source, provide a link to the Creative Commons licence, and indicate if changes were made. The images or other third party material in this article are included in the article's Creative Commons licence, unless indicated otherwise in a credit line to the material. If material is not included in the article's Creative Commons licence and your intended use is not permitted by statutory regulation or exceeds the permitted use, you will need to obtain permission directly from the copyright holder. To view a copy of this licence, visit <http://creativecommons.org/licenses/by/4.0/>.

© The Author(s) 2026